Hyaluronic acid biosynthesis promotes an invasive, stem-like cancer cell phenotype by broadly altering metabolism.

Adrian A. Shimpi[1*], Matthew L. Tan[1*], Michael Vilkhovoy[2], David Dai[2], L. Monet Roberts[1, 2], Joe Kuo[2], Lingting Huang[2], Jeffrey D. Varner[2], Matthew Paszek[2,3], Claudia Fischbach[1,3,†]

[1]Nancy E. and Peter C. Meinig School of Biomedical Engineering, Cornell University, Ithaca, New York, 14853, USA

[2]Robert Frederick Smith School of Chemical and Biomolecular Engineering, Cornell University, Ithaca, New York, 14853, USA

[3]Kavli Institute at Cornell for Nanoscale Science, Cornell University, Ithaca, New York, 14853, USA

*Contributed equally to this work

[†]Corresponding author:

Claudia Fischbach-Teschl

cf99@cornell.edu

The authors declare no potential conflicts of interest.

Word Count: 4034 without Abstract and Materials and Methods

Figures and Tables: 6 main figures, 7 supplementary figures, 1 supplementary table, 3 supplementary files

Abstract

Metastasis is the leading cause of breast cancer-related deaths and driven by invasion, but how cancer stem-like cells (CSCs) and their metabolic phenotype regulate breast cancer invasion remains unclear. Using microfluidic invasion models, metabolomics, and computational flux balance analysis (FBA), we investigated the functional links between the stem-like, metabolic, and invasive phenotype of breast cancer cells. Our results suggest that CSCs are more invasive than non-CSCs and that broad metabolic changes associated with overproduction of hyaluronic acid (HA) rather than transcriptional changes caused by hypoxia-inducible factor 1α (HIF1α)-related signaling play a role in this process. Accordingly, overexpression of hyaluronic acid synthases (HAS) 2 or 3 induced a breast cancer metabolic phenotype that promoted stemness and invasion. These changes were clinically significant as a gene signature defined by HAS2/3 overexpression correlated with increased invasion and was predictive of worse patient survival. Collectively, this study suggests that HA overproduction enabled by metabolic reprogramming negatively influences prognosis in breast cancer patients by enhancing stemness and invasion and expands the current paradigm implicating HIF1α signaling as the major driver of these processes.

Introduction

Despite advancements in treatment options, breast cancer remains the second leading cause of cancer-related deaths in women[1]. Mortality in breast cancer is driven by metastasis and relapse, during which cancer cells in the primary tumor invade into surrounding tissues and disseminate into distant sites to form secondary tumors. Recent studies suggests that this process is mediated by a subpopulation of cancer cells known as cancer stem-like cells (CSCs)[2]. CSCs are characterized by the expression of stem-cell associated markers (e.g. NANOG, SOX2, OCT4, aldehyde dehydrogenase [ALDH]) self-renewal properties, and increased invasiveness that collectively promote tumor metastasis and subsequent relapse[3,4]. However, mechanisms that contribute to the emergence and maintenance of the CSC phenotype with consequences on tumor invasion are poorly understood.

Aberrant cellular metabolism is one of the hallmarks of cancer and has historically been described as the Warburg effect where cancer cells undergo glycolytic metabolism despite the presence of oxygen[5]. However, it is now clear that tumor cells are metabolically plastic allowing them to dynamically adapt their metabolism to accommodate spatiotemporal changes in oxygen and nutrient availability[6]. Furthermore, CSCs exhibit metabolic phenotypes distinct from non-CSCs, which influences their ability to maintain redox homeostasis providing attractive therapeutic targets[7–9]. How metabolic reprogramming promotes or maintains stem-like properties in breast cancer cells and which consequences these changes have on tumor invasion, however, remains unclear.

Increased hyaluronic acid (HA) production can induce a CSC phenotype, and previous studies suggest that metabolic flux into the hexosamine biosynthesis pathway (HBP) and corresponding changes in hypoxia-inducible factor 1α (HIF1α) signaling play a role in this process[10]. Whether or not HA biosynthesis affects metabolism more broadly, however, remains undefined due to limited methods that allow studies of metabolism at the scale of genome-wide networks. Accumulation of HA and increased expression of HA synthase 2 (HAS2) and glutamine:fructose-6-phosphate amidotransferase 1 (GFAT1), the rate-limiting enzyme of HBP, have been correlated with worse breast cancer patient survival[11–13]. These results suggest a prominent role for HAS2, but HA is produced by several HAS isoforms that vary in enzyme kinetics, nutrient sensitivity, and the formation of microvilli-like structures on the cell surface suggestive of differences in cell-surface retention[14–17]. Moreover, clinical studies suggest that increased HA production irrespective of the HAS isoform is associated with worse tumor differentiation[11,12]. Which role HAS isotype-independent metabolic reprogramming plays in this process, how HA overproduction affects metabolism besides altering HBP and HIF1α, and which effect these changes have on the CSC phenotype and invasion have been understudied.

Here, we use a combination of engineered cell lines, microfabricated culture models, computational approaches, and patient survival analysis to investigate the interconnectedness of the CSC phenotype, HA production, and metabolism and its influence on cancer cell invasion. We demonstrate that increased HA production promotes stemness due to broad metabolic changes. These changes stimulate cancer cell invasive potential irrespective of HAS isoform and were associated with worse patient survival. Collectively, our results suggest that HA

overproduction due to metabolic reprogramming negatively influences prognosis in breast cancer patients by altering invasion.

Results

Cancer Stem-Like Cells Exhibit Increased Invasive Potential

To investigate differences in invasion between CSCs and their non-differentiated counterparts, we utilized the CSC reporter cell line GFP-NANOG MDA-MB-231 in which green fluorescent protein (GFP) expression is controlled by the NANOG promoter[18] (Fig. 1a). Using fluorescence-activated cell sorting (FACS) GFP-NANOG MDA-MB-231 cells were sorted into GFP^{Null}, GFP^{Low} (bottom 5% GFP expressing), and GFP^{High} (top 5% GFP expressing cells) populations to enrich for different stem-like states (Fig. 1a) whose phenotype was maintained over 5 days of culture (Supplementary Fig. 1). Moreover, the GFP^{High} cell population proliferated more slowly than the non-CSC GFP^{Null} population, consistent with a more quiescent phenotype (Fig. 1b). To study potential differences in the invasive phenotype of these different cell populations, we monitored tumor cell invasion in response to a morphogen gradient using a microfluidic collagen type I hydrogel model (Fig. 1c). In this setup, GFP^{High} NANOG MDA-MB-231 cells invaded into the 3D collagen hydrogel region of the device more readily than their less stem-like counterparts, validating that CSCs exhibit increased invasive potential (Fig. 1c,d). Cell migration and invasion are energetically intensive processes requiring increased metabolic consumption[19]. Accordingly, inhibiting energy production with the glycolysis inhibitor 2-deoxyglucose (2-DG) reduced both collagen hydrogel invasion and random 2D migration of unsorted GFP-NANOG MDA-MB-231 cells (Fig. 1e,f). These results indicate that CSCs exhibit increased invasive and migratory potential in our experimental setup that was dependent on glycolytic metabolism.

Cancer Stem-Like Cells Have Altered Metabolism

To characterize the metabolic phenotype of cancer cells as a function of their stem-like phenotype, extracellular metabolite production and consumption rates were measured in sorted GFP-NANOG cells (Fig. 2a,b). The more stem-like cells consumed more glucose and produced more lactate relative to their non-stem-like counterparts indicative of increased glycolysis (Fig. 2a). Real-time metabolic analysis with the Agilent Seahorse (Seahorse) Analyzer of extracellular acidification rate (ECAR) and oxygen consumption rate (OCR) further suggested that CSCs not only exhibited increased glycolysis, but also oxidative phosphorylation (Fig. 2b, Supplementary Fig. 2). Acccordingly, culturing in glucose-free media decreased the percentage of GFP^{High} cells relative to media containing physiological levels of glucose (Fig. 2c). This approach also decreased the ALDH bright ($ALDH^{Br}$) fraction (a marker for breast CSCs[20,21]) of wildtype MDA-MB-231 cells confirming that our results were not an artefact of the GFP-NANOG reporter cell line. Moreover, inhibition of glycolysis by 2-DG reduced the GFP^{High} population further corroborating that the CSC phenotype is intimately linked to glucose metabolism (Fig. 2d).

As increased HA production has been associated with both metabolic reprogramming and the CSC phenotype[10,13], we next assessed how HA production correlates with the CSC phenotype. Immunofluorescence (IF) image analysis identified that GFP expression in GFP-NANOG MDA-MB-231 cells positively correlated with the amount of cell surface-associated HA (Fig. 2e). These differences were likely due to changes in HA biosynthesis and subsequent cell surface retention as analysis of secreted HA by ELISA indicated low levels across all experimental

conditions that were not significantly different from each other although more stem-like cells seemed to secrete slightly less HA (Supplementary Fig. 3a). Together, these results suggest that more stem-like cells exhibit increased glucose metabolism relative to their less stem-like counterparts and that these changes correlate with elevated levels of cell surface-associated HA.

Hyaluronic Acid Production Correlates with Stemness

To better quantify the relationship between glucose metabolism, cell surface-associated HA, and stemness, GFP-NANOG MDA-MB-231 cells were stained for HA and then subjected to flow cytometry and targeted metabolomics. Consistent with the IF results, the amount of cell surface-associated HA directly correlated with GFP expression levels (Fig. 3a). Importantly, sorting the GFP-NANOG MDA-MB-231 cells into high and low HA producing cells for targeted metabolomics revealed broad changes of intracellular metabolites with hierarchical clustering separating the two HA production phenotypes (Fig. 3b). In particular, both upper glycolytic and tricarbocylic acid (TCA) cycle metabolites such as glucose-6-phosphate (G6P), fructose-6-phosphate (F6P), oxaloacetate (OAA), and citrate (CIT) were increased in the highly HA producing cells (Fig. 3c). Combining these results with the broad metabolic alterations of CSCs described above (Fig. 2), these data suggest a direct link between glycolysis-dependent HA synthesis and the CSC phenotype (Fig. 3d). To more directly test how HA synthesis affects stemness, GFP-NANOG MDA-MB-231 cells were cultured with the HA synthesis inhibitor 4-methylumbelliferone (4-MU, 0.5 mM). This approach resulted in a decrease of stem-like GFP^{High} cells consistent with previous studies using primary murine breast cancer cells cells[22] (Supplementary Fig. 3b). However, this effect was not significant in our hands possibly due to

differences in the utilization of UDP-glucuronic acid (UDP-GlcUA, a subunit of HA) by different cell lines[23], which is depleted by 4-MU treatment[24].

To more directly determine if increasing production of HA promotes stemness, HAS2 and HAS3 were stably overexpressed in MDA-MB-231 and the non-malignant breast epithelial cell line MCF10A. While HA is synthesized by three HAS isoforms (HAS1, 2, 3), HAS 1 varies in HA synthesis and secretion rate from HAS 2 and 3. In contrast, HAS2 and HAS3 exhibit similar sensitivities and responses to precursor availability and thus were used here to study their effects on the metabolic reprogramming[14–16]. Overexpression of HAS2/3 increased the defining characteristic of CSCs in both cell lines: self-renewal as measured through sphere formation in a limited dilution assay (Fig. 3e, Supplementary Fig. 4a,b). Additionally, overexpression of both HAS2/3 markedly increased the fraction of $CD44^{+}/CD24^{-}$ MCF10A cells, which characterizes an invasive breast CSC population with more mesenchymal characteristics[25,26] (Fig. 3f, Supplementary Fig. 4d). This population could not be assessed in HAS overexpressing MDA-MB-231 as this cell line contains an intrinsically high fraction of CD44+/CD24- cells (>85%), making changes difficult to quantify[27,28] (Supplementary Fig. 4c). Nevertheless, HAS3 overexpression increased the $ALDH^{Br}$ fraction in MCF10A, albeit in a non-statistically significant trend (Supplementary Fig. 4e). Together, these results suggest that HA overproduction increases stem-like cell properties in breast cancer cells regardless of cell line and HAS2/3 isoform.

Increased HA Production by CSCs is Associated with Increased Glucose Conversion and ATP Production

Given our results that metabolic reprogramming of CSCs supports their energy demands during invasion (Fig. 2) and that a more stem-like phenotype is associated with increased HA production (Fig. 3), we speculated that increased HA production promotes a more energetic CSC phenotype. Probing the individual contribution of HA biosynthetic pathways to the metabolic state of CSCs solely by measuring different metabolite levels, however, is challenging given the interconnectedness of most metabolic pathways. To circumvent these limitations and delineate the contribution of HA biosynthesis to CSC metabolism more directly, a flux balance analysis (FBA) model was constructed. FBA is a widely utilized mathematical approach to model the flow of metabolites (flux) through a genome-scale network of metabolic pathways, including glycolysis, oxidative phosphorylation, hexosamine biosynthesis, and amino acid consumption[29], and has been successfully used to investigate cancer metabolism[30,31]. In contrast to traditional metabolomics, FBA also enables the simulation of a desired metabolic phenotype by adjusting model parameters such as the objective function and flux constraints. To develop the model for our study, extracellular metabolomics of GFP^{High} and GFP^{Null} cells were performed over 72 hours to define metabolite consumption/production profiles used to constrain flux values for more and less stem-like MDA-MB-231 breast cancer cells, respectively (Fig. 4a). Additionally, the objective function of the FBA model was set to maximize HA synthesis to study both the capacity of CSCs and non-CSCs to produce HA and the associated changes in metabolic flux. Results from the FBA model indicated that the more stem-like cells (GFP^{High}) increased flux through the upper stages of glycolysis (i.e., conversion of glucose to fructose-6-phosphate), ATP generation, lactate production/secretion, and glutamine uptake relative to the non-stem-like cells (GFP^{Null}) (Fig. 4b, Supplementary File 1). Additionally, the FBA model indicated increased flux through all HA synthesis intermediate steps for the GFP^{high} cells relative to the GFP^{null} cells (Fig.

4c). Collectively, these data suggest that the increased capacity of CSCs to synthesize HA is related to increased glucose conversion but simultaneously allows these cells to produce ATP more efficiently. To confirm the predictive value of the FBA model, a Seahorse real-time ATP rate assay was performed. This analysis verified that the mitochondrial and overall ATP production rate was increased in GFP^{High} versus GFP^{Null} cells (Fig. 4d,e). Together, these findings suggest that the metabolic phenotype of more stem-like cancer cells leading to increased HA biosynthesis promotes ATP production by these cells. FBA models are suitable for predicting these changes.

Metabolic Changes resulting from Increased HA Production Stimulate a Stem-like Breast Cancer Cell Phenotype to Promote Invasion.

Our aforementioned results suggest functional links between the stem-like and invasive phenotype of tumor cells (Fig. 1), CSCs and metabolism (Fig. 2), CSCs and HA (Fig. 3), and HA and metabolism (Fig. 4). Furthermore, HA has been previously associated with increased invasion[32,33]. However, whether or not these single observations are mechanistically connected remained to be determined. Therefore, we next hypothesized that the metabolic phenotype induced by HA overproduction increases the stem-like phenotype of breast cancer cells to promote invasion. Indeed, Seahorse analysis revealed that MCF10A and MDA-MB-231 cells overexpressing HAS2 and HAS3 had increased ECAR compared to their parental controls suggesting an increase in glycolytic energy production (Fig. 5a). Interestingly, OCR was unchanged in HAS2/3-overexpressing MCF10A but increased in HAS2/3-overexpressing MDA-MB-231 cells (Supplementary Fig. 5a), consistent with an increase in OCR in GFP^{High} vs. GFP^{Low} and GFP^{Null} MDA-MB-231 (Fig. 2b). Treatment with 2-DG decreased both cell surface-

associated and secreted HA in MCF10A cells (Supplementary Fig. 5b, c). Notably, 2-DG treatment of MCF10A cells decreased the $CD44^+/CD24^-$ fraction in the HA overproducing cells but had no effect on the parental control cells suggesting that the enhanced glycolysis associated with HA overproduction is critical to maintaining stemness (Fig. 5b). Furthermore, HA overproduction increased both total and glycolytic ATP production (Fig. 5c, Supplementary Fig. 5d) that 2-DG reversed to similar levels as in MCF10A control cells (Fig. 5c). A similar trend was noted for MDA-MB-231 cells, although 2-DG decreased glycolytic ATP production only in the HAS3 overexpressing cells. Overexpression of HAS2/3 also increased invasion of both MCF10A and MDA-MB-231 (Fig. 5d, e), consistent with their increased stem-like phenotype (Fig. 3d, e). This effect was inhibited by 2-DG treatment, implicating a functional consequence of HA-mediated stemness and metabolism in tumor cell invasion (Fig. 5d, e). As 2-DG treatment did not affect the ATP production rate in parental cells (Fig. 5c), these changes in invasion can be attributed to differences in metabolism rather than compromised cell viability. Together this data suggests that HA overproduction induces a glycolytic phenotype that is crucial for CSC-mediated invasion.

HA Overproduction Transcriptome Changes Predict Worse Patient Survival

Our data suggest that both HAS2 and 3 induce phenotypes associated with increased invasion and, thus, malignancy. RNA sequencing was conducted on the MCF10A cells overexpressing HAS2 and HAS3 and their parental control to identify transcriptional changes that would allow us to interrogate the contribution of HA overproduction to stemness, invasion, and patient outcomes. Principle component analysis (PCA) and hierarchical clustering indicated that the transcriptome of HA overproducing cells differed significantly from their parental control (Fig.

6a, b, Supplementary Fig. 6a, Supplementary File 2). Gene set enrichment analysis (GSEA) with the Hallmarks gene sets from the Molecular Signature Database revealed enrichment of a wide range of pathways for both HAS2 and HAS3-overexpressing cells, including those previously associated with stemness and invasion such as NF-κB[34], hypoxia[35], PI3K signaling[36], IL6-STAT3 signaling, and reactive oxygen species[7,8] (Fig 6c). Since HIF1α signaling has been previously implicated in an HA-dependent increase in the CSC phenotype[10], we performed GSEA for HIF1α target genes[37–41]. Interestingly, neither HAS2 nor HAS3 transcriptomes were enriched for HIF1α target genes (Fig. 6d), which have previously been suggested as drivers of HA-dependent stemness[10]. These results further support our findings that the cellular phenotypes investigated in this study are due to broader metabolic changes and cannot be attributed to glycolysis-driven changes in hypoxia-related signaling.

To determine the clinical relevance of our findings, a 72-gene signature was generated from the genes upregulated in both HAS2 and HAS3-overexpressing cells ($\log_2$-fold change > 1, p-value < 0.05) compared to their parental control (Fig. 6e, Supplementary Table 1). Overrepresentation analysis of this gene signature surprisingly revealed no significant enrichment of genes associated with most metabolic pathways from the KEGG database (Supplementary Fig. 6b) possibly due to the fact that energy production can be regulated beyond transcriptional changes[42,43]. Subsequently, we calculated enrichment scores for this HA overproduction gene signature and a curated list of gene signatures involved in migration, cytoskeleton dynamics, and metabolism (Supplementary File 3, Supplementary Fig. 7a) using single sample GSEA (ssGSEA)[44] for chemotherapy-naïve patients in the METABRIC cohort. Tumorous tissue from patients enriched for our HA overproduction signature were simultaneously enriched for several

migration and actin cytoskeleton gene sets suggesting increased tumor invasion in these patients, while metabolic gene sets unrelated to glycosaminoglycan synthesis were not enriched after correcting for random associations (Fig. 6f, Supplementary Fig. 7b,c). Importantly, our HA overproduction signature also predicted worse patient survival consistent with their increased expression of invasion-related gene sets (Fig. 6f,g). Gene signatures specific to upregulation of either HAS2 or HAS3 also predicted worse patient survival that was not seen in the parental control (Supplementary Fig. 6c). Collectively, our results suggest that genes associated with increased HA biosynthesis correlate with an enrichment of migratory genes and predict worse patient survival regardless of HAS2/3 isoform.

Discussion

Although CSCs are known to exhibit a distinct metabolic phenotype from non-CSCs, the exact nature of their metabolic alterations and consequences on tumor invasion, a hallmark of metastasis and worse patient prognosis, remain unclear. Indeed, past studies have reported that CSCs have either a primarily glycolytic phenotype[9,45] or increased mitochondrial oxidative metabolism[46,47]. Furthermore, the functional link between CSC metabolism and invasion is understudied although invasion is known to be a highly energetic process and is often driven by more stem-like cancer cells. Here, we demonstrate that CSCs can increase glycolytic and oxidative metabolism simultaneously and that these changes in metabolism promote stemness and invasion due to increased HA production. Moreover, we identified that these cellular changes correlated with a gene expression signature that was independent of differential expression of HIF1α target genes, but predictive of patient survival.

The energetic demands associated with HA-mediated invasion can induce broad metabolic changes. For example, increased HA production rapidly depletes UDP-sugar substrates, which cancer cells may compensate for by increasing glycolysis to maintain flux into the HBP and thus, the pool of UDP-sugars[10]. Our FBA model corroborates this phenomenon and provides further insight into metabolic states associated with CSCs such as an increased HA production capacity. The resulting metabolic phenotypes associated with overexpressing HAS2 or HAS3 in cells suggest that the glycolytic demand dominates over possible changes in oxidative metabolism previously associated with stemness[8,48,49]. Furthermore, our finding that HA overproduction induces phenotypic and transcriptomic changes that correlate with invasion may help explain why glycolytic, mesenchymal breast CSCs localize to the leading edge of tumors and worsen patient prognosis[8,26]. Together, these results suggest that HA production enables a more invasive, malignant CSC metabolic phenotype.

To interrogate alterations in other metabolic pathways associated with glycolysis and oxidative phosphorylation, we utilized FBA to predict changes in metabolic fluxes induced by stemness. FBA is especially proficient in enabling the study of cancer metabolism as it simulates metabolic phenotypes based on real-world constraints such as cell growth rate and glucose uptake[29,50]. The FBA model developed here indicated that stem-like cells exhibited an increased capacity for HA production, and that this increase in HA production was associated with broad metabolic alterations. Interestingly, our model suggested that although the conversion of glucose to pyruvate is decreased in stem-like cells when maximizing HA production, the production of both lactate and acetyl-CoA from pyruvate is increased. An alternative source of pyruvate are the malic enzymes, which convert malate to pyruvate while producing the reducing agent NADPH[51].

Indeed, our FBA model indicated an increase in the flux through malic enzyme 2 (ME2), which operates within the mitochondria (Supplementary File 1). Increased ME2 activity has been previously associated with the loss of cellular senescence and increased tumorigenesis[52,53]. Additionally, ME2 plays a crucial role in the production of glutamine which provides a source of n-acetylglucosamine, one of the building blocks of HA[54]. The FBA model developed here supports our results that CSCs are associated with increased HA production and energy production. However, any connection with malic enzyme activity will need to be experimentally verified in future experiments, as is typical in interpreting FBA predictions.

Throughout the metastatic cascade, HA has been implicated in promoting invasive phenotypes and to support survival of circulating cells in the vasculature[32,33,55]. While HA-dependent changes of cancer malignancy and stemness have been primarily attributed to upregulation of HAS2[13,22], our results indicate that HAS3 similarly promotes a stem-like state (Fig. 3). Indeed, the fact that 2-DG inhibited the tumor cell stem-like phenotype in both HAS2/3-overexpressing cells suggests that the metabolic reprogramming enacted by HA overproduction may be the central regulator of the tumor stem-like phenotype (Fig. 5b). HA production is regulated by cytoplasmic pools of UDP sugars, which are elevated in cancerous breast tissue[56,57]. The conversion of UDP-glucose to UDP-glucuronic acid can regulate metastasis through *SNAI1* mRNA stabilization[58], which we identified as upregulated in HA overproducing cells (Fig. 6, Supplementary File 2). Interestingly, degradation of HA produced by cancer cells promotes glucose uptake that can promote migration and further fuel metabolism[59]. Combined with our results, this suggests HA intermediates generated by HA-induced metabolic reprogramming may

help regulate metastatic phenotypes, but further experiments delineating the contributions of HA-associated metabolic intermediates on the CSC phenotype are required.

Transcriptomic analysis of HAS2 and HAS3 overexpressing MCF10As indicated an enrichment of multiple stemness-associated gene sets (e.g. IL6-JAK-STAT3 signaling and hypoxia), but metabolic genes were not differentially expressed. This discrepancy with our experimental observations may be explained by the fact that metabolic changes are not only regulated transcriptionally but also by enzyme activity levels and localization[42,43]. For example, the activity of phosphofructokinase (PFK), a key enzyme controlling glycolytic flux[60], is regulated by glycosylation with O-linked β-N-acetylglucosamine (O-GlcNAc)[61]. Our FBA model indicates that CSCs have an increased HBP capacity to produce UDP-GlcNAc, the sugar donor for O-GlcNAcylation, which would be expected to decrease PFK activity and thus glycolysis[61]. Instead, our results suggest an increase rather than decrease in glycolysis, possibly because flux rates are not regulated soley by cytoplasmic enzymes levels, but also through their relative activities and substrates availability[42,60,62]. Furthermore, cytoskeletal rearrangement, which is critical for invasion, can independently control glycolytic flux by mediating enzyme degradation[63] or sequestration[43]. Our results suggest that the glycolytic CSC phenotype associated with HA overproduction is not regulated transcriptionally, but whether this is enacted by cytoskeletal dynamics or changes in the relative activity of different metabolic enzymes requires further investigation.

Our data suggests that cell states associated with increased glycolysis enrich for highly invasive CSCs that are characterized by increased HA production. Interestingly, HA produced by CSCs is

primarily retained on the cell surface rather than excreted into the surrounding environment (Fig. 3, Supplementary Fig. 3). Consequentially, the retention of HA on the cell surface contributes to glycocalyx thickness whose biophysical properties impact the interactions between cells and their surrounding environment including cell-extracellular matrix interactions necessary for migration[17,64]. In particular, HA-dependent changes of the glycocalyx can promote adhesion-independent or ameboid migration by altering the friction required for force generation against extracellular structures[65]. Alternatively, changes in glycocalyx thickness impact surface receptor diffusion patterns and generate kinetic traps that lead to receptor clustering to strengthen adhesion assembly and activate mechanosignaling[66,67]. Further studies to delineate the contributing biophysical properties are needed to determine the influence of HA on predominant migration mode. Moreover, migration is an energy-intensive process and the necessary ATP utilization can determine migration decisions. Therefore, the increased ATP production observed in the stem-like and HA-overproducing cells highlights the need to decouple glycocalyx-mediated, biophysical determinants from metabolic reprogramming. Overall our results provide a possible explanation for why CSCs are associated with increased metastasis. Nevertheless, further characterization of the biophysical and metabolic phenotype of CSCs and their contributions to invasion and metastasis are necessary to define additional therapeutic targets.

Acknowledgements

Thank you to all members of the Fischbach lab for valuable feedback and discussion of the research. The authors would also thank Dr. Andrea Di Micheli, David McKellar, and Dr. Ben Cosgrove for assistance with RNA-sequencing data processing. The work described was supported by National Cancer Institute through the Center on the Physics of Cancer Metabolism

(1U54CA210184), the National Science Foundation (NSF) through Graduate Research Fellowship Program awarded to A.A.S and L.M.R. (DGE-1650441), the U.S. Department of Education through the Graduate Assistance in Areas of National Need (GAANN) Fellowship awarded to M.L.T., the Breast Cancer Coalition of Rochester, and the Cornell NanoScale Science & Technology Facility (CNF), a member of the National Nanotechnology Coordinated Infrastructure (NNCI) supported by the National Science Foundation (Grant NNCI-2025233). This work utilized facilities at the Cornell Institute of Biotechnology including the Cornell University Biotechnology Resource Center (BRC) Imaging Facility (RRID:SCR_021741) for image acquisition using the Zeiss LSM 710 Confocal Microscope (NIH 1S10RR025502), the BRC Genomics Facility (RRID:SCR_021727) for sequencing, and the BRC Flow Cytometry Facility (RRID:SCR_021740) for cell sorting with BD Biosciences FACSAria Fusion. Mass spectrometric analysis of targeted metabolomics was performed at the Weill Cornell Medicine Proteomics and Metabolomics Core Facility.

Author Contributions

A.A.S., M.L.T., and C.F. designed the study. A.A.S. and M.L.T. conducted most of the experiments. M.V. and D.D. conducted extracellular metabolomics for FBA analysis. L.M.R. and M.P. performed FACS for HA production. J.K., L.H., and M.P. generated plasmids for HAS overexpression. L.M.R. and A.A.S. generated cell lines. J.V. and M.L.T. performed FBA analysis. A.A.S., M.L.T., and C.F. analyzed the data and wrote the manuscript. All authors discussed the results and commented on the manuscript.

Materials and Methods

Cell Culture

MCF10A (ATCC) cells were cultured in DMEM/F12 supplemented with 5% Horse Serum, 1% penicillin/streptomycin, 10 µg/mL Insulin, 0.5 µg/mL Hydrocortisone, 100 ng/mL Cholera toxin, and 20 ng/mL human epidermal growth factor (EGF). MDA-MB-231 (ATCC) and the GFP-NANOG MDA-MB-231 (a kind gift from Dr. Ofer Reizes[18]) cells were cultured in DMEM supplemented with 10% FBS and 1% penicillin/streptomycin. HAS overexpressing cells were cultured in their respective medias containing 1 µg/mL doxycycline (Santa Cruz Biotechnology). For glycolytic inhibition studies, cells were treated with media containing 2-deoxyglucose (MilliporeSigma) matching the glucose concentration in the media (25mM or 20mM for DMEM, DMEM/F12 respectively) for 24 hours unless otherwise noted.

Generated Cell Lines

cDNAs for human HAS2 and HAS3 were generated and cloned into the lentiviral vector pLV HygroR tetOn to create stably transduced, tetracycline-inducible MCF10A cell lines as previously described[17]. cDNAs for human HAS2 and HAS3 were also fabricated and inserted into a tetracycline-inducible PiggyBac expression vector to generate pPB huHAS2-IRES2-mScarlet-IRES2-NeoR and pPB huHAS3-IRES2-mScarlet-IRES2-NeoR through custom gene synthesis (Twist Biosience). Generation of the MDA-MB-231 HAS overexpressing cells was conducted using either the pPB huHAS2-IRES2-mScarlet-IRES2-NeoR or pPB huHAS3-IRES2-mScarlet-IRES2-NeoR or with the Piggybac transponase using the Nucleofector Cell Line Kit V (Lonza). Stably transfected cells were selected using 1 µg/mL puromycin (MilliporeSigma) or 800 µg/mL G418 (ThermoFisher). MDA-MB-231 HAS overexpressing cells were then sorted post-selection on mScarlet expression levels.

FACS and Flow Cytometry

GFP-NANOG MDA-MB-231 cells were trypsinized and resuspended at $10x10^6$ cells/mL in FACS buffer (2.5% FBS/PBS, 2mM EDTA) and processed on the BD FACSAria Fusion Cell Sorter. The top 5% and bottom 5% of the GFP+ fraction were designated as GFP^{High} and GFP^{Low} respectively, while the non-GFP expressing population were designated as GFP^{Null}. Cells were sorted into cell culture media, recounted, seeded, and allowed to rest for 24 hours before use in experiments.

Cell sorting for targeted metabolomics was conducted on GFP-NANOG MDA-MB-231 cells stained for HA using Alexfluor-568 (ThermoFisher) conjugated HA binding protein (HABP, 40 µg/mL, MilliporeSigma). The high HA (top 5%) or low HA (bottom 5%) fractions were sorted using a BD FACSAria Fusion Cell Sorter.

ALDH activity was determined for MDA-MB-231 and MCF10A cells using the Aldefluor™ Assay (STEMCELL Technologies) according to manufacturer instructions with incubation conducted for 30min at 37°C. Analysis was conducted on a BD Accuri C6 Plus analyzer.

The fraction of CD44+/CD24- cells was determined by trypsinizing and resuspending cells in FACS buffer at $10x10^6$ cells/mL followed by incubation with antibodies against human CD44 (APC-conjugated, Clone G44-26, 1:5, BD Biosciences) and CD24 (PE-Cy7-conjugated, Clone ML5, 1:20, BD Biosciences). Gates were determined using the isotype controls mouse anti-IgG2b κ (APC-conjugated, Clone 27-35, 1:5, BD Biosciences) and mouse anti-IgG2a κ (PE-Cy7-conjugated, Clone G155-178, 1:20, BD Biosciences). Cells were analyzed on a BD Accuri C6 Plus Analyzer.

Invasion and Migration Assays

To prepare microfluidic invasion assays, rat tail Type I collagen (Corning) was neutralized with 1 N NaOH and diluted with 1X DMEM to a final concentration of 2.5 mg/mL. Before neutralization and dilution, 10x DMEM was added to collagen as a pH indicator to a final concentration of 10% v/v. Microfluidic 3D cell culture devices (AIM Biotech) were then injected with the 2.5 mg/mL rat tail Type I collagen solution into the center channel of the chip. The chips were then incubated at 4°C for 30 minutes, followed by incubation at 37°C for 30 minutes to complete collagen polymerization. For MDA-MB-231 invasion, DMEM containing 1% FBS and 1% penicillin/streptomycin was injected into the left flanking media channel, and DMEM containing 10% FBS and 1% penicillin/streptomycin was injected into the right flanking media channel. For MCF10A invasion, MCF10A media devoid of Horse Serum and EGF was injected into the left flanking media channel, and fully supplemented MCF10A media was injected into the right flanking media channel. 10 μL of a 2.5×10^5 cell suspension of GFP-NANOG MDA-MB-231 or MCF10A cells were then injected into both ports of the left channel (20 μL total). Cells were allowed to invade through the hydrogel channel for 3 - 5 days before fixation in a 4% paraformaldehyde solution. Media was exchanged every 24 hours. After fixation, chips were stained, imaged, and individual cell invasion distance was measured using ImageJ by segmenting nuclei.

To assess random migration ability, GFP-NANOG MDA-MB-231 cells were plated on fibronectin-coated (30 μg/mL) glass 96 well plates and placed in an Incucyte S3 (Sartorius) live cell imaging system. Images were obtained in 20-minute intervals over 24 hours. Individual cell tracking was performed using ImageJ to determine migration velocity (motility) and random migration paths.

Immunofluorescence

GFP-NANOG MDA-MB-231 cells were plated on fibronectin-coated (30 µg/mL) glass coverslips at 2500 cells/cm^2. Cells were then fixed in 4% paraformaldehyde (PFA)/PBS (w/v) for 20 min at room temperature, blocked with 1% bovine serum albumin (BSA)/PBS (w/v) for 1 hr at room temperature, and incubated overnight with AlexaFluor-568 conjugated hyaluronic acid binding protein (HABP, 13.3 µg/mL, MilliporeSigma) at 4°C. Afterwards cells were incubated with DAPI (2.5 µg/mL, ThermoFisher) for 30 min at room temperature.

For invasion experiments, devices were fixed in 4% paraformaldehyde (PFA)/PBS for 30 min at room temperature, permeabilized with 0.1% Triton X-100/PBS (v/v) for 15 min at room temperature, blocked with 1% bovine serum albumin (BSA)/PBS (w/v) for 1 hr at room temperature, and incubated with DAPI (2.5 µg/mL) and either AlexaFluor-568 (ThermoFisher) or AlexaFluor-647 (ThermoFisher) phalloidin to visualize F-actin.

Confocal Microscopy and Image Analysis

Images were acquired on a Zeiss LSM 710 confocal microscope with either a LD LCI Plan-Apochromat 25×/0.8 Imm Korr DIC M27 or C-Apochromat W M27 10x/0.45 objective. Images were analyzed using ImageJ with custom scripts. Briefly, for single cell intensity measurements, z-stacks were sum projected and cells were segmented based on HA intensity. Cell clusters were manually corrected to individual cells, while overlapping or edge-located cells were excluded from analysis.

For invasion experiments, the C-Apochromat W M27 10x/0.45 objective was used at 0.6x zoom, and a z-stack was obtained along a 2 mm length in the center of the device. Z-stacks were

maximum intensity projected, and invasion was assessed based on nuclei displacement along the x-axis (across the hydrogel region). Invasion distance was normalized to the appropriate control in each set of replicates per experiment, and data was pooled together across device replicates to obtain averages per condition.

Metabolic Analysis

To obtain an initial measure of glycolytic ability, sorted GFP-NANOG MDA-MB-231 cells were seeded in 24 well plates at 10,000 cells/cm^2 in 1 mL of media. Glucose concentration was measured using a GlucCell Glucose Monitoring System (CESCO Bioengineering), and lactate concentration was obtained using a colormetric lactate assay kit (Sigma).

Targeted metabolomics was conducted on GFP-NANOG MDA-MB-231 cells 48 hours post sorting for HA production. Media was collected and non-adherent cells were pelleted at 500 x g for 4 minutes. Meanwhile, 0.5 mL of 80% methanol (MetOH) was added onto adherent cells and incubated at -80°C, After aspirating supernatant, the cell pellet was resuspended in 0.5 mL of 80% MetOH and added to the respective well of adherent cells in plate and incubated at -80°C for 15 minutes. Cells were then scraped using a cell scraper and collected into an Eppendorf tube and pelleted at 20,000 x g for 10 minutes at 4°C. Supernatant was then transferred to 2 mL screw-cap vial and dried overnight under vaccum at room temperature. Following overnight drying, samples were then dried for 2.5 hours in SpeedVac SPD 1030 at room temperature and then stored at -80°C until analyzed by Weill Cornell Medicine Proteomics and Metabolomics Core Facility.

Real-time changes in metabolism were tested using a Seahorse XFe96 Analyzer in conjunction with the Seahorse XF Glycolysis Stress Test Assay Kit and the Seahorse XF Real-time ATP

Assay Rate Kit (Agilent). Manufacturer instructions were followed to perform each of the assays. Wildtype and modified MDA-MB-231 cells were seeded on a Seahorse XFe96 Cell Culture microplate at 20,000 cells per well in standard media and allowed to attach overnight. For experiments with MCF10A, cells were seeded at 20,000 cells per well. HAS overexpressing cells had media changed 24 hours after seeding to include 1 μg/mL doxycycline. Media was then changed to the specific Seahorse assay media, and plates were prepared according to manufacturer instructions for each assay kit. Relevant metabolic values from each assay were calculated using template worksheets provided by Agilent. After the assays were complete, DNA was extracted from each well using Caron's Buffer (25 mM Tris-HCl, 0.4 M NaCl, 0.5% (w/v) sodium dodecylsulfate), and total DNA content measured using the fluorometric Quantifluor dsDNA Assay (VWR) and converted to cell number for normalization.

Flux Balance Analysis (FBA)

To generate a computational model of metabolic fluxes in sorted GFP-NANOG MDA-MB-231 cells, cells were sorted as described above and seeded into 24 well plates at 10,000 cells/cm^2. Cells were allowed to attach overnight before a fresh media change. Media was collected 72 hours after the initial media change and stored at -80°C before performing extracellular metabolomics to measure levels of glucose, lactate, and the 20 amino acids. Glucose was measured using Contour next EZ Blood Glucose Monitoring System (Ascensia Diabetes Care) using 5 μL as the sample volume. Lactate and amino acid concentrations were assayed using an Acquity UPLC H-Class System equipped with QDa and tunable UV (TUV) detectors controlled by Empower 3 software (Waters Corporation). Specifically, extracellular amino acids were analyzed using a Waters AccQ-Tag Ultra Derivatization Kit (Waters) according to the

manufacturer's recommendations. Derivatized samples were injected onto an AccQ-Tag Ultra C18 column (1.7 μm, 2.1 mm x 100 mm, Waters) and detected by an Acquity TUV detector (Waters) at 260 nm. Amino acids were identified by known retention times of standards and concentrations were determined by comparison with calibration standard curves. For the lactate measurements, samples were first deproteinized by treatment with an equal volume of trichloroacetic acid followed by centrifugation at 12,000 x g for 10 minutes. 200 μL of the supernatant was then combined with 600 μL of acetonitrile (ACN) before injecting 2 μL into the LC-MS system. Lactate was quantified using a standard curve ranging from 0.05mM to 1mM. Separations were performed on an Acquity UPLC BEH Amide Column (1.7 μm, 2.1 mm x 100 mm, Waters). Solvent A consisted of 50:50 ACN:Water and solvent B consisted of 95:5 ACN:Water. The solvent gradient started at 0.01% solvent A and 99.9% solvent B, raised to 40% A in 0.5 minutes, further raised to 70% A in 1.5 minutes, and returned to initial conditions over 0.1 minute and held for 3 minutes to re-equilibrate the column. The flow rate was set to 0.6 mL/min, the autosampler was set to 5°C, and the column was set to 50°C. The mass-to-charge ratio (m/z) of lactate was 88.9. Analysis was performed in negative ion mode with a cone voltage of 15V and probe temperature of 600°C.

Extracellular metabolomics data of all 20 amino acids, lactate, and glucose was then used to constrain a flux balance analysis by imposing bounds on allowable fluxes. Growth rate and O2 fluxes were constrained from cell counts and Seahorse data respectively. The model used in this study was implemented in the Julia programming language[68], where the linear programming problem was solved using the GNU Linear Programming Kit (GLPK) package (https://www.gnu.org/software/glpk/). The stoichiometric matrix and metabolic growth requirements were derived from a previously developed Core Cancer model[31]. The objective

function was set to maximize HA production subject to experimentally estimated rates of uptake, secretion, and cell growth to define the phenotype of interest; 1000 simulations were performed for each condition. A subset of the FBA results representing the energetic pathways of interest was incorporated into a graphical representation (Fig. 4). The full FBA results can be found in Supplementary File 1.

Limited Dilution Assay

Cells were serially diluted and seeded into ultra-low attachment 96-well plates (Corning) in 200 μL of serum-free DMEM/F-12 containing 2% B27, 10 ng/mL basic fibroblast growth factor, 20 ng/mL epidermal growth factor, 10 μg/mL insulin, and 1 μg/mL doxycycline. Sphere formation was assessed after two weeks of culture, and the number of spheres was counted using a phase-contrast microscope. The stem cell frequency was determined using the extreme limited dilution algorithm[69].

RNA-Sequencing

Parental (NeoR-rtTA) and HA overproducing MCF10A cells were seeded on 10-cm dishes at 5000 cells/cm^2 and allowed to adhere overnight. Media was refreshed to include 1 μg/mL of doxycycline to induce HAS2 and HAS3 expression and cultured for an additional 48 hours. RNA was isolated using the Qiagen RNeasy kit according to manufacturer instructions. RNA libraries were prepared using the Illumina TruSeq RNA Kit, and single-ended 75bp read lengths were sequenced on the Illumina NextSeq 500 system.

Sequence Alignment and Gene Set Enrichment Analysis

Reads were trimmed using TrimGalore version 0.4.4 (https://www.bioinformatics.babraham.ac.uk/projects/trim_galore/) and aligned to the human reference genome GRCh38 (ENSEMBL) using STAR version 2.6.0a[70]. Reads of genomic features were counted using featureCounts[71], and differential gene expression was determined using DESeq2[72]. Differentially expressed genes in HA overproducing cells were defined as a log-2 fold change greater than 1 and an adjusted p-value less than 0.0001 compared to the parental cells. Genes common to both HAS2 and HAS3 were combined to generate the HA overproducing gene signature for survival analysis. Individual HAS2 and HAS3 gene signatures were defined as the differentially expressed genes with log 2-fold change greater than 2 or 5, respectively, and a p-value less than 0.0001.

Gene set enrichment analysis (GSEA) was conducted with a ranked list generated by taking the sign of the fold change multiplied by the log-10 of the adjusted p-value. The list was inputted to the GSEA Java applet (http://software.broadinstitute.org/gsea/index.jsp) using the GSEAPreRanked tool and the Hallmarks gene sets from MSigDB v.7.0. Gene sets were considered significantly enriched with a p-value and FDR value ≤ 0.05.

Patient Survival and Enrichment Analysis

Patient data from the METABRIC cohort was extracted from the Cancer Genomics Data Server. Patients were limited to those having not received chemotherapy. Gene signature scores were calculated using the single-sample GSEA (ssGSEA)[44] with the GSVA package[73]. The top and bottom quartiles of the ssGSEA scores for the 72-gene HA overproduction signature were designated as high and low scores, respectively, for survival and enrichment analysis. Kaplan-Meier survival analysis was conducted with the *survival* package in R using a Cox proportional

hazard model with statistical significance determined using a log-rank test. Stratified patients were further analyzed for enrichment of curated lists of migration, cytoskeletal, and metabolic gene signatures obtained from the MSigDB v7.0. To correct for random associations, 300 randomly selected gene signatures with the same number of genes (15-500 genes) as gene sets in the curated list had ssGSEA enrichment scores additionally calculated. An empricial cumulative distribution function was established using the *ecdf* function in R and a p-value cutoff was determined where 95% of values fell below.

Statistical analysis

All experiments were performed with at least three independent biological replicates unless otherwise noted. Pairwise comparisons were conducted using a Mann-Whitney U test unless otherwise noted. Multiple comparisons were evaluated with either a Kruskal-Wallis Test or two-way ANOVA with Dunn's post hoc analysis. Results were considered statistically significant with a p-value less than 0.05. Unless otherwise noted, all data points are plotted mean +/- the standard deviation. All statistically analysis was performed using GraphPad Prism v9.3 or R.

References

1. Siegel, R. L., Miller, K. D. & Jemal, A. Cancer statistics, 2020. *CA. Cancer J. Clin.* **70**, 7–30 (2020).

2. Batlle, E. & Clevers, H. Cancer stem cells revisited. *Nat. Med.* **23**, 1124–1134 (2017).

3. Pattabiraman, D. R. & Weinberg, R. A. Tackling the cancer stem cells — what challenges do they pose? *Nat. Rev. Drug Discov.* **13**, 497–512 (2014).

4. Wu, C.-W. (Ken), Wang, M.-L. & Chiou, S.-H. Targeting cancer stem cells: emerging role of Nanog transcription factor. *Onco. Targets. Ther.* **6**, 1207 (2013).

5. DeBerardinis, R. J. & Chandel, N. S. Fundamentals of cancer metabolism. *Sci. Adv.* **2**,

e1600200 (2016).

6. Fendt, S.-M., Frezza, C. & Erez, A. Targeting Metabolic Plasticity and Flexibility Dynamics for Cancer Therapy. *Cancer Discov.* **10**, 1797–1807 (2020).

7. Diehn, M. *et al.* Association of reactive oxygen species levels and radioresistance in cancer stem cells. *Nature* **458**, 780–783 (2009).

8. Luo, M. *et al.* Targeting Breast Cancer Stem Cell State Equilibrium through Modulation of Redox Signaling. *Cell Metab.* **28**, 69-86.e6 (2018).

9. Peiris-Pagès, M., Martinez-Outschoorn, U. E., Pestell, R. G., Sotgia, F. & Lisanti, M. P. Cancer stem cell metabolism. *Breast Cancer Res.* **18**, 55 (2016).

10. Chanmee, T. *et al.* Hyaluronan Production Regulates Metabolic and Cancer Stem-like Properties of Breast Cancer Cells via Hexosamine Biosynthetic Pathway-coupled HIF-1 Signaling. *J. Biol. Chem.* **291**, 24105–24120 (2016).

11. Auvinen, P. *et al.* Hyaluronan in Peritumoral Stroma and Malignant Cells Associates with Breast Cancer Spreading and Predicts Survival. *Am. J. Pathol.* **156**, 529–536 (2000).

12. Auvinen, P. *et al.* Hyaluronan synthases (HAS1–3) in stromal and malignant cells correlate with breast cancer grade and predict patient survival. *Breast Cancer Res. Treat.* **143**, 277–286 (2014).

13. Chokchaitaweesuk, C., Kobayashi, T., Izumikawa, T. & Itano, N. Enhanced hexosamine metabolism drives metabolic and signaling networks involving hyaluronan production and O-GlcNAcylation to exacerbate breast cancer. *Cell Death Dis.* **10**, 803 (2019).

14. Itano, N. *et al.* Three Isoforms of Mammalian Hyaluronan Synthases Have Distinct Enzymatic Properties. *J. Biol. Chem.* **274**, 25085–25092 (1999).

15. Rilla, K. *et al.* Hyaluronan Synthase 1 (HAS1) Requires Higher Cellular UDP-GlcNAc Concentration than HAS2 and HAS3*. *J. Biol. Chem.* **288**, 5973–5983 (2013).

16. Rilla, K. *et al.* Hyaluronan production enhances shedding of plasma membrane-derived microvesicles. *Exp. Cell Res.* **319**, 2006–2018 (2013).

17. Shurer, C. R. *et al.* Physical Principles of Membrane Shape Regulation by the Glycocalyx. *Cell* **177**, 1757-1770.e21 (2019).

18. Thiagarajan, P. S. *et al.* Development of a Fluorescent Reporter System to Delineate Cancer Stem Cells in Triple-Negative Breast Cancer. *Stem Cells* **33**, 2114–2125 (2015).

19. Romani, P., Valcarcel-Jimenez, L., Frezza, C. & Dupont, S. Crosstalk between mechanotransduction and metabolism. *Nat. Rev. Mol. Cell Biol.* **22**, 22–38 (2021).

20. Ginestier, C. *et al.* ALDH1 Is a Marker of Normal and Malignant Human Mammary Stem

Cells and a Predictor of Poor Clinical Outcome. *Cell Stem Cell* **1**, 555–567 (2007).

21. Vincent, K. M., Findlay, S. D. & Postovit, L. M. Assessing breast cancer cell lines as tumour models by comparison of mRNA expression profiles. *Breast Cancer Res.* **17**, 114 (2015).

22. Chanmee, T. *et al.* Excessive Hyaluronan Production Promotes Acquisition of Cancer Stem Cell Signatures through the Coordinated Regulation of Twist and the Transforming Growth Factor β (TGF-β)-Snail Signaling Axis. *J. Biol. Chem.* **289**, 26038–26056 (2014).

23. Kultti, A. *et al.* 4-Methylumbelliferone inhibits hyaluronan synthesis by depletion of cellular UDP-glucuronic acid and downregulation of hyaluronan synthase 2 and 3. *Exp. Cell Res.* **315**, 1914–1923 (2009).

24. Kakizaki, I. *et al.* A Novel Mechanism for the Inhibition of Hyaluronan Biosynthesis by 4-Methylumbelliferone. *J. Biol. Chem.* **279**, 33281–33289 (2004).

25. Al-Hajj, M., Wicha, M. S., Benito-Hernandez, A., Morrison, S. J. & Clarke, M. F. Prospective identification of tumorigenic breast cancer cells. *Proc. Natl. Acad. Sci.* **100**, 3983–3988 (2003).

26. Liu, S. *et al.* Breast Cancer Stem Cells Transition between Epithelial and Mesenchymal States Reflective of their Normal Counterparts. *Stem Cell Reports* **2**, 78–91 (2014).

27. Li, W. *et al.* Unraveling the roles of CD44/CD24 and ALDH1 as cancer stem cell markers in tumorigenesis and metastasis. *Sci. Rep.* **7**, 13856 (2017).

28. Sheridan, C. *et al.* CD44+/CD24-breast cancer cells exhibit enhanced invasive properties: an early step necessary for metastasis. *Breast Cancer Res.* **8**, R59 (2006).

29. Orth, J. D., Thiele, I. & Palsson, B. Ø. What is flux balance analysis? *Nat. Biotechnol.* **28**, 245–248 (2010).

30. Asgari, Y., Zabihinpour, Z., Salehzadeh-Yazdi, A., Schreiber, F. & Masoudi-Nejad, A. Alterations in cancer cell metabolism: The Warburg effect and metabolic adaptation. *Genomics* **105**, 275–281 (2015).

31. Zielinski, D. C. *et al.* Systems biology analysis of drivers underlying hallmarks of cancer cell metabolism. *Sci. Rep.* **7**, 1–14 (2017).

32. Brett, M.-E. *et al.* In vitro elucidation of the role of pericellular matrix in metastatic extravasation and invasion of breast carcinoma cells. *Integr. Biol.* **10**, 242–252 (2018).

33. Offeddu, G. S. *et al.* The cancer glycocalyx mediates intravascular adhesion and extravasation during metastatic dissemination. *Commun. Biol.* **4**, 255 (2021).

34. Korkaya, H., Liu, S. & Wicha, M. S. Breast cancer stem cells, cytokine networks, and the tumor microenvironment. *J. Clin. Invest.* **121**, 3804–3809 (2011).

35. Pang, M.-F. *et al.* Tissue Stiffness and Hypoxia Modulate the Integrin-Linked Kinase ILK to Control Breast Cancer Stem-like Cells. *Cancer Res.* **76**, 5277–5287 (2016).

36. Yoon, C. *et al.* PI3K/Akt pathway and Nanog maintain cancer stem cells in sarcomas. *Oncogenesis* **10**, 12 (2021).

37. Liberzon, A. *et al.* The Molecular Signatures Database Hallmark Gene Set Collection. *Cell Syst.* **1**, 417–425 (2015).

38. Miroshnikova, Y. A. *et al.* Tissue mechanics promote IDH1-dependent HIF1α–tenascin C feedback to regulate glioblastoma aggression. *Nat. Cell Biol.* **18**, 1336–1345 (2016).

39. Schaefer, C. F. *et al.* PID: the Pathway Interaction Database. *Nucleic Acids Res.* **37**, D674–D679 (2009).

40. Semenza, G. L. Hypoxia-inducible factor 1: oxygen homeostasis and disease pathophysiology. *Trends Mol. Med.* **7**, 345–350 (2001).

41. Slemc, L. & Kunej, T. Transcription factor HIF1A: downstream targets, associated pathways, polymorphic hypoxia response element (HRE) sites, and initiative for standardization of reporting in scientific literature. *Tumor Biol.* **37**, 14851–14861 (2016).

42. Hackett, S. R. *et al.* Systems-level analysis of mechanisms regulating yeast metabolic flux. *Science (80-.).* **354**, aaf2786–aaf2786 (2016).

43. Hu, H. *et al.* Phosphoinositide 3-Kinase Regulates Glycolysis through Mobilization of Aldolase from the Actin Cytoskeleton. *Cell* **164**, 433–446 (2016).

44. Barbie, D. A. *et al.* Systematic RNA interference reveals that oncogenic KRAS-driven cancers require TBK1. *Nature* **462**, 108–112 (2009).

45. Chen, C.-L. *et al.* NANOG Metabolically Reprograms Tumor-Initiating Stem-like Cells through Tumorigenic Changes in Oxidative Phosphorylation and Fatty Acid Metabolism. *Cell Metab.* **23**, 206–219 (2016).

46. Pastò, A. *et al.* Cancer stem cells from epithelial ovarian cancer patients privilege oxidative phosphorylation, and resist glucose deprivation. *Oncotarget* **5**, 4305–4319 (2014).

47. Vlashi, E. *et al.* Metabolic differences in breast cancer stem cells and differentiated progeny. *Breast Cancer Res. Treat.* **146**, 525–534 (2014).

48. Dong, C. *et al.* Loss of FBP1 by Snail-Mediated Repression Provides Metabolic Advantages in Basal-like Breast Cancer. *Cancer Cell* **23**, 316–331 (2013).

49. Ciavardelli, D. *et al.* Breast cancer stem cells rely on fermentative glycolysis and are sensitive to 2-deoxyglucose treatment. *Cell Death Dis.* **5**, e1336–e1336 (2014).

50. Lewis, N. E. & Abdel-Haleem, A. M. The evolution of genome-scale models of cancer metabolism. *Front. Physiol.* **4**, 1–7 (2013).

51. Simmen, F. A., Alhallak, I. & Simmen, R. C. M. Malic enzyme 1 (ME1) in the biology of cancer: it is not just intermediary metabolism. *J. Mol. Endocrinol.* **65**, R77–R90 (2020).

52. Jiang, P., Du, W., Mancuso, A., Wellen, K. E. & Yang, X. Reciprocal regulation of p53 and malic enzymes modulates metabolism and senescence. *Nature* **493**, 689–693 (2013).

53. Cheng, C.-P. *et al.* The mechanisms of malic enzyme 2 in the tumorigenesis of human gliomas. *Oncotarget* **7**, 41460–41472 (2016).

54. Sarfraz, I. *et al.* Malic enzyme 2 as a potential therapeutic drug target for cancer. *IUBMB Life* **70**, 1076–1083 (2018).

55. Turley, E. A., Wood, D. K. & McCarthy, J. B. Carcinoma Cell Hyaluronan as a "Portable" Cancerized Prometastatic Microenvironment. *Cancer Res.* **76**, 2507–2512 (2016).

56. Oikari, S. *et al.* UDP-sugar accumulation drives hyaluronan synthesis in breast cancer. *Matrix Biol.* **67**, 63–74 (2018).

57. Caon, I. *et al.* Sirtuin 1 reduces hyaluronan synthase 2 expression by inhibiting nuclear translocation of NF-κB and expression of the long-noncoding RNA HAS2–AS1. *J. Biol. Chem.* **295**, 3485–3496 (2020).

58. Wang, X. *et al.* UDP-glucose accelerates SNAI1 mRNA decay and impairs lung cancer metastasis. *Nature* **571**, 127–131 (2019).

59. Sullivan, W. J. *et al.* Extracellular Matrix Remodeling Regulates Glucose Metabolism through TXNIP Destabilization. *Cell* **175**, 117-132.e21 (2018).

60. Tanner, L. B. *et al.* Four Key Steps Control Glycolytic Flux in Mammalian Cells. *Cell Syst.* **7**, 49-62.e8 (2018).

61. Yi, W. *et al.* Phosphofructokinase 1 Glycosylation Regulates Cell Growth and Metabolism. *Science (80-.).* **337**, 975–980 (2012).

62. Liberti, M. V. *et al.* A Predictive Model for Selective Targeting of the Warburg Effect through GAPDH Inhibition with a Natural Product. *Cell Metab.* **26**, 648-659.e8 (2017).

63. Park, J. S. *et al.* Mechanical regulation of glycolysis via cytoskeleton architecture. *Nature* **578**, 621–626 (2020).

64. Kuo, J. C.-H., Gandhi, J. G., Zia, R. N. & Paszek, M. J. Physical biology of the cancer cell glycocalyx. *Nat. Phys.* **14**, 658–669 (2018).

65. Bergert, M. *et al.* Force transmission during adhesion-independent migration. *Nat. Cell Biol.* **17**, 524–529 (2015).

66. Paszek, M. J. *et al.* The cancer glycocalyx mechanically primes integrin-mediated growth and survival. *Nature* **511**, 319–325 (2014).

67. Barnes, J. M. *et al.* A tension-mediated glycocalyx–integrin feedback loop promotes mesenchymal-like glioblastoma. *Nat. Cell Biol.* **20**, 1203–1214 (2018).

68. Bezanson, J., Edelman, A., Karpinski, S. & Shah, V. B. Julia: A Fresh Approach to Numerical Computing. *SIAM Rev.* **59**, 65–98 (2017).

69. Hu, Y. & Smyth, G. K. ELDA: Extreme limiting dilution analysis for comparing depleted and enriched populations in stem cell and other assays. *J. Immunol. Methods* **347**, 70–78 (2009).

70. Dobin, A. *et al.* STAR: ultrafast universal RNA-seq aligner. *Bioinformatics* **29**, 15–21 (2013).

71. Liao, Y., Smyth, G. K. & Shi, W. featureCounts: an efficient general purpose program for assigning sequence reads to genomic features. *Bioinformatics* **30**, 923–930 (2014).

72. Love, M. I., Huber, W. & Anders, S. Moderated estimation of fold change and dispersion for RNA-seq data with DESeq2. *Genome Biol.* **15**, 550 (2014).

73. Hänzelmann, S., Castelo, R. & Guinney, J. GSVA: gene set variation analysis for microarray and RNA-Seq data. *BMC Bioinformatics* **14**, 7 (2013).

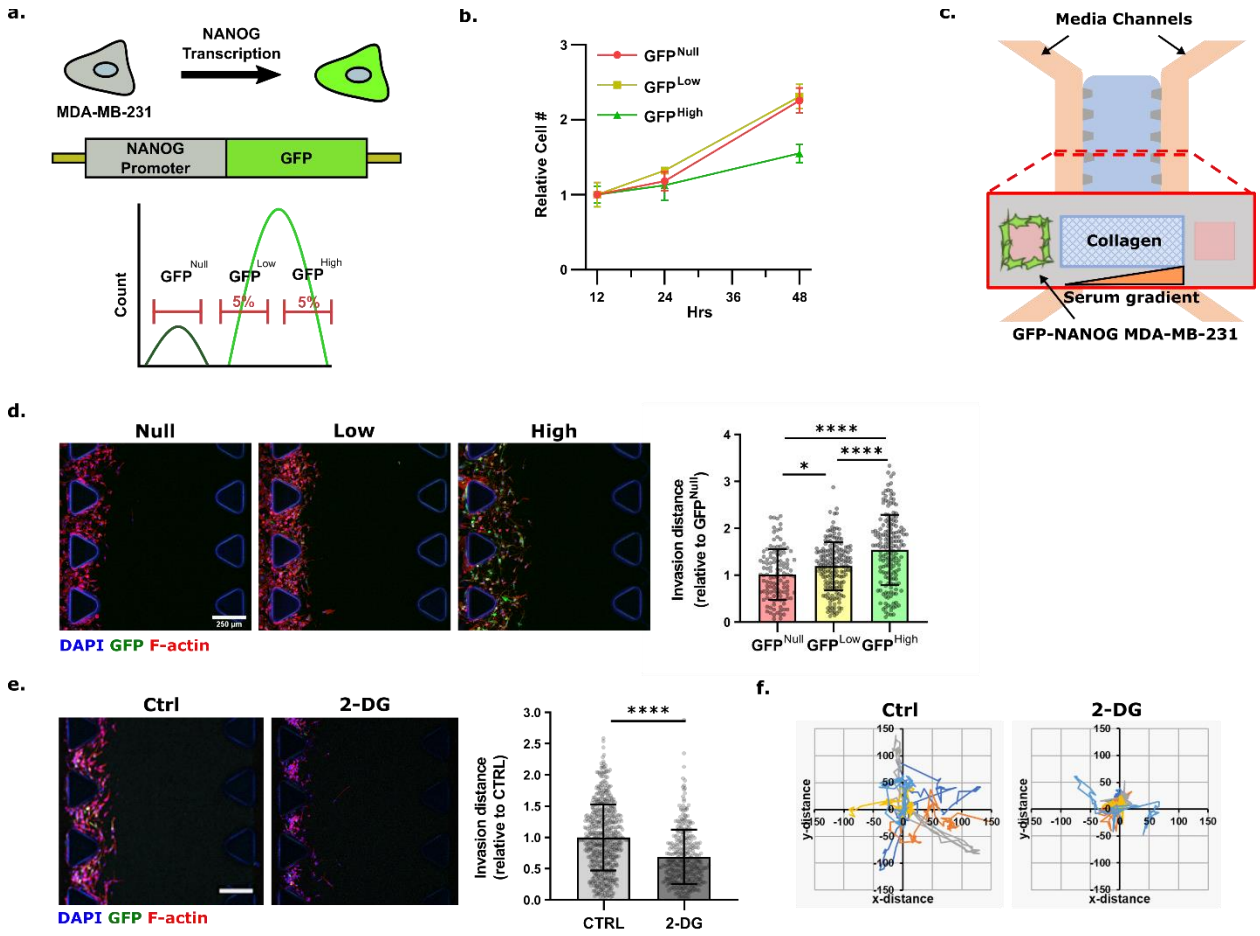

Figure 1: CSCs have increased invasive potential that is sensitive to metabolic challenge. a) Schematic of the cancer stem cell reporter line GFP-NANOG MDA-MB-231 and sorting strategy. **b)** Growth curve of sorted cells as measured by DNA amount, normalized to the first measurement at t = 12 hrs (n = 3 samples). **c)** Schematic of the microfluidic device to analyze cell invasion in response to a morphogen gradient generated by applying serum-containing medium to the right channel only. **d)** Invasion distance of sorted GFP-NANOG MDA-MB-231 into collagen type I over 5 days (n = 4 fields of views, 1 device per condition). **e)** Invasion of GFP-NANOG MDA-MB-231 cells into collagen type I treated with or without 2-DG for 5 days (n = 3 devices per condition). **f)** Random migration of GFP-NANOG MDA-MB-231 treated with or without 2-DG for 24 hours (n = 5 representative cells for migration plots, n = 20 cells per condition for motility). Scale bar = 250 µm. * $p < 0.05$, ** $p<0.01$, *** $p<0.001$, **** $p<0.0001$

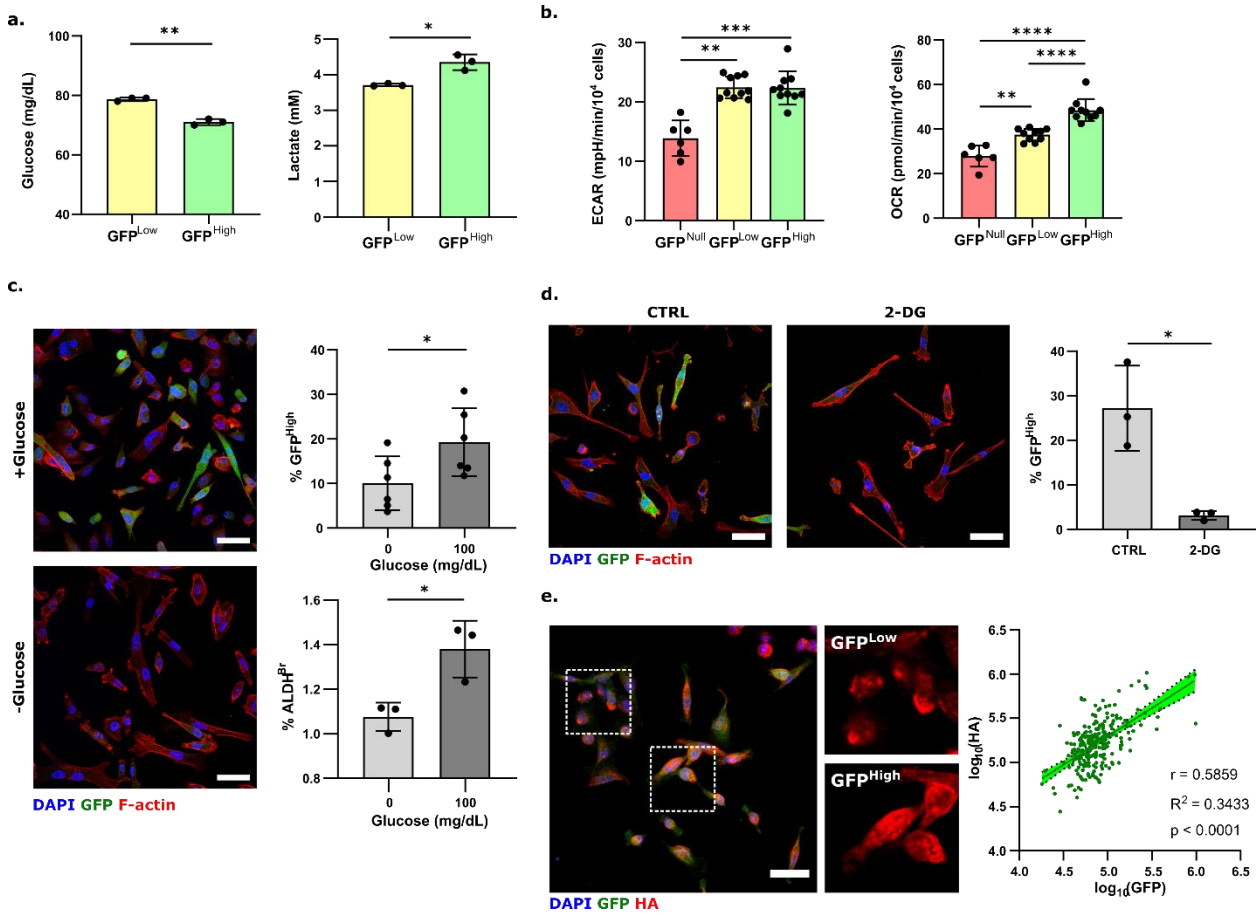

Figure 2: Cancer stem-like cells exhibit altered metabolism compared to non-stem-like cancer cells. a) Glucose and lactate concentrations in media conditioned by sorted GFP-NANOG MDA-MB-231 cells 48 hrs post sort as measured by a GlucCell glucose meter and a lactate colorimetric assay (n = 3 samples). **b)** ECAR and OCR measurements of sorted GFP-NANOG cells obtained during Seahorse-based glycolysis stress test (n > 6 samples). **c)** Fraction of GFP positive (GFP+) GFP-NANOG MDA-MB-231 (n = 6) (i) and aldehyde dehydrogenase high (ALDH+) (n = 3) (ii) parental MDA-MB-231 when cultured with 100 mg/dL glucose (+glucose) or glucose-free media (-glucose) for 72 hours. GFP+ and ALDH+ cells were determined by image analysis and Aldefluor assay, respectively. **d)** Fraction of GFP+ GFP-NANOG MDA-MB-231 cells treated with or without 2-deoxyglucose (2-DG) (n = 3). **e)** Immunofluorescence analysis of HA in the MDA-MB-231 NANOG reporter line. (n = 248 cells) Scale bar = 50 μm. * $p < 0.05$, ** $p<0.01$, *** $p<0.001$, **** $p<0.0001$.

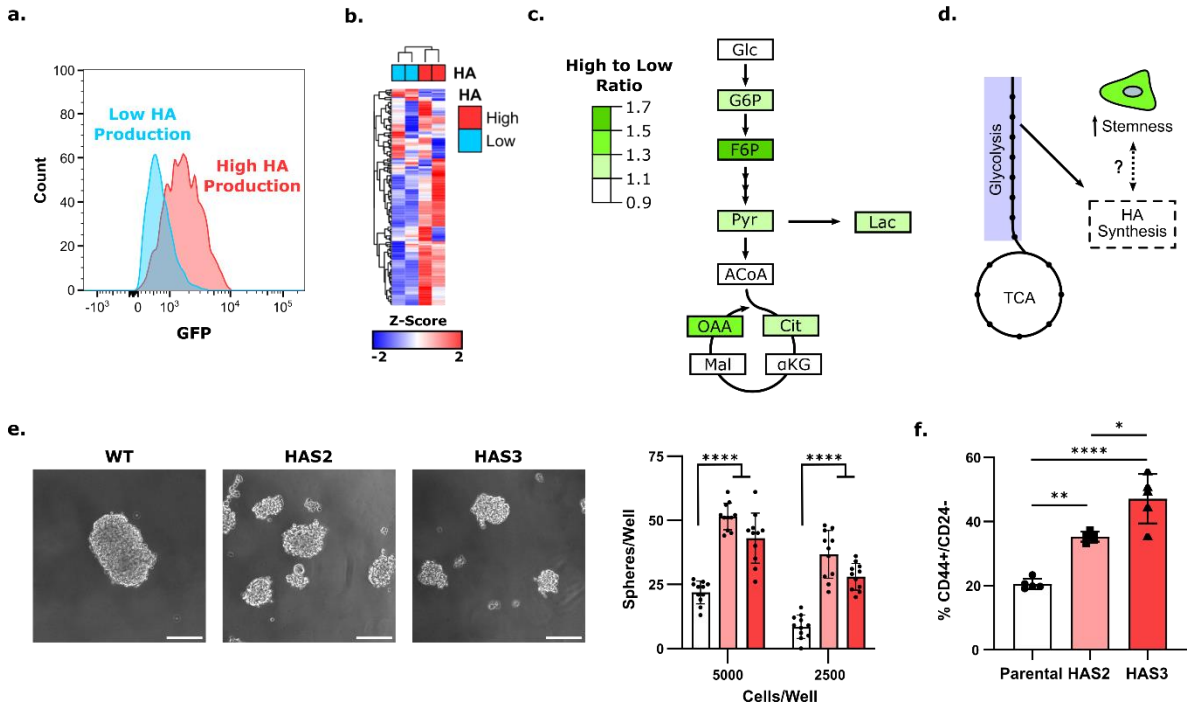

Figure 3: Increased HA production correlates with an increase in CSCs. a) Flow cytometry analysis of cellular GFP levels categorized by their levels of cell surface-associated HA. **b)** Heatmap representing changes of intracellular metabolites as measured by metabolomics of sorted HA^{High} and HA^{Low} GFP-NANOG MDA-MB-231. **c)** Graphical representation of selected metabolites in the central carbon metabolic pathway ratios between HA^{High} and HA^{Low} cells. **d)** Schematic representing the theorized relationship between glycolysis, HA synthesis, and stemness. **e)** Representative images of spheres formed through a limiting dilution assay of HAS2 and HAS3 overexpressing MDA-MB-231 and the corresponding sphere number. (n = 11) **f)** Flow cyometry analysis of the percentage of the $CD44^{+}/CD24^{-}$ population of parental or HA overproducing MCF10A cells (n = 5). * $p<0.05$, ** $p< 0.01$, **** $p<0.001$. Scale bar = 200 μm.

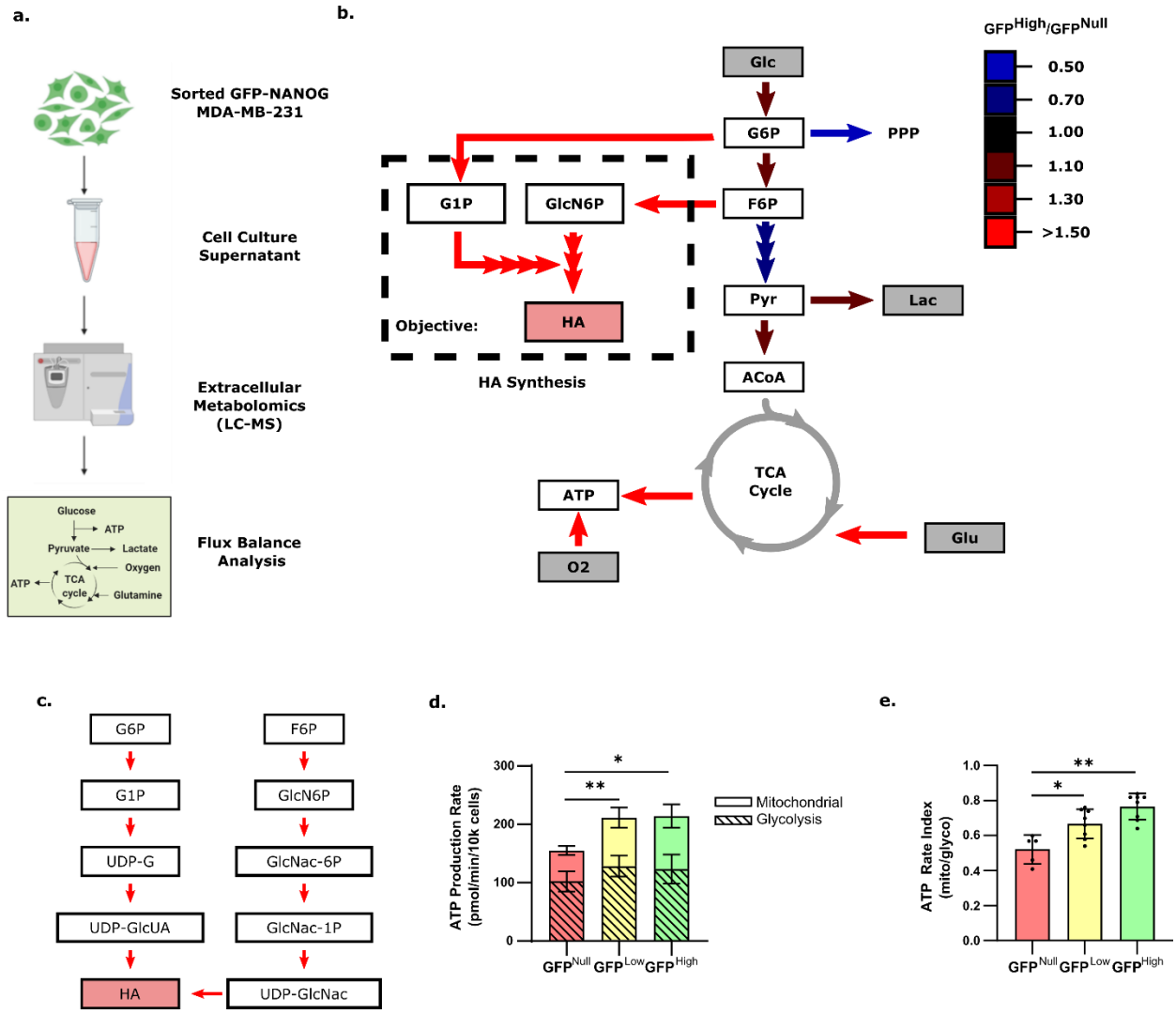

Figure 4: Flux balance analysis predicts increased HA production in cancer stem-like cells and ATP production. a) Workflow schematic. Sorted GFP-NANOG cells were cultured for 72 hrs before performing extracellular metabolomics using LC-MS. This data was used to constrain a computational flux balance analysis model. **b)** Flux balance analysis model of the bioenergetic pathway of sorted GFP-NANOG MDA-MB-231 derived from extracellular metabolomics obtained over 72 hours of culture. Fluxes shown are GFP^{High} relative to GFP^{Null}. Grey metabolites indicate relevant metabolite fluxes constrained based on extracellular metabolomic profiles. Oxygen was constrained using values obtained from the Agilent Seahorse assay. For the total FBA model constraints and results, see Supplementary File 1. **c)** Expanded HA synthesis pathway flux balance analysis of GFP^{High} relative to GFP^{Null} (dashed box in B). Same legend as in B. **d)** ATP production rate and **e)** rate index derived from measurements using the Agilent Seahorse ATP real-time production rate assay kit ($n \geq 5$). * $p<0.05$, ** $p< 0.01$.

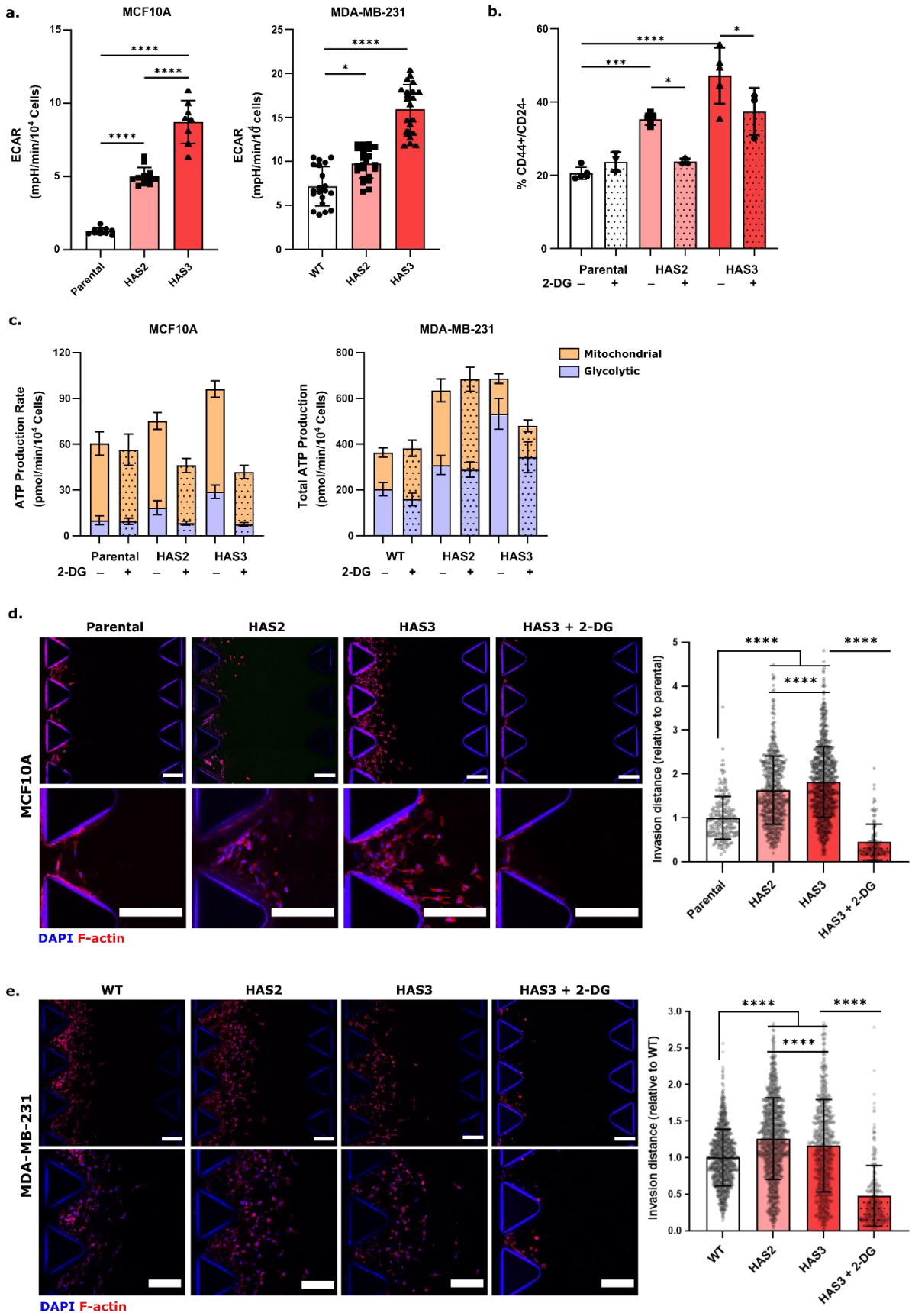
a.
MCF10A
MDA-MB-231
ECAR (mpH/min/10⁴ Cells)
ECAR (mpH/min/10⁴ cells)
Parental
HAS2
HAS3
WT
b.
% CD44+/CD24-
2-DG
c.
ATP Production Rate (pmol/min/10⁴ Cells)
Total ATP Production (pmol/min/10⁴ Cells)
Mitochondrial
Glycolytic
d.
Parental
HAS2
HAS3
HAS3 + 2-DG
MCF10A
Invasion distance (relative to parental)
DAPI F-actin
e.
WT
MDA-MB-231
Invasion distance (relative to WT)

Figure 5: Increased glycolytic metabolism necessary for HA production stimulates stemness and invasion of breast cancer cells. a) Extracellular acidification rate measurements of parental MCF10A or HA overproducing cells using the Agilent Seahorse XF Analyzer. **b)** Percentage of $CD44^+/CD24^-$ cells of parental MCF10A or HA overproducing cells with or without 20mM 2-DG as measured by flow cytometry. **c)** ATP production rate of either MCF10A or MDA-MB-231 cells overexpressing HAS2 or HAS3 pre-treated with or without 2-DG (20mM for MCF10A, 25mM for MDA-MB-231) as measured using the Real-Time ATP Rate Assay in the Agilent Seahorse XF Analyzer. ($n \geq 8$) **d)** Invasion of the MCF10A and **e)** MDA-MB-231 HA overproducing cells. Representative immunofluorescence images and corresponding quantification of invasion after 5 days are shown (n = 3 devices per condition). Scale bar: 200 μm, * $p < 0.05$, ** $p<0.01$, *** $p<0.001$, **** $p<0.0001$

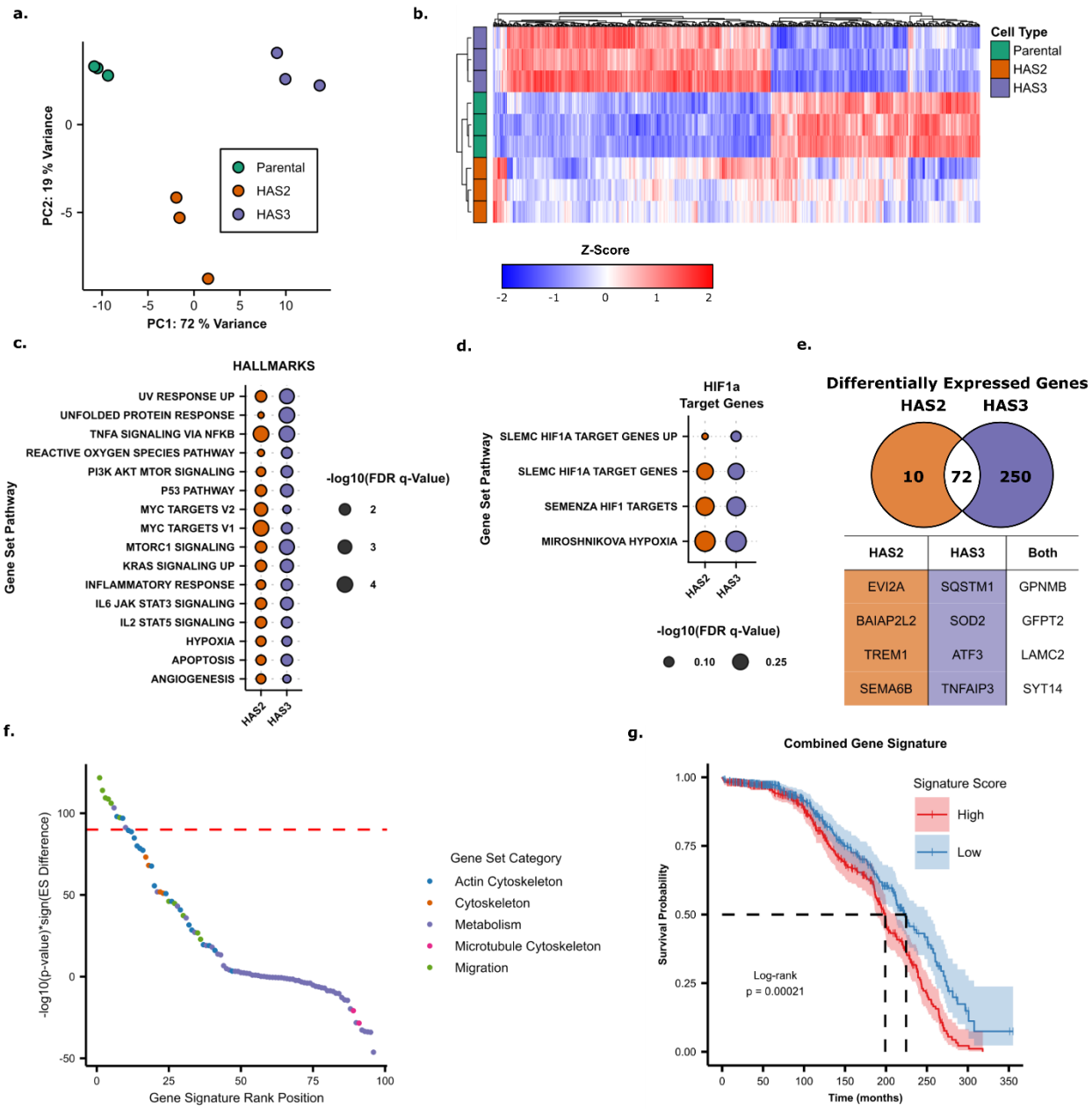

Figure 6: Gene signatures of HA overproducing cells correlate with worse patient prognosis regardless of HAS isoform. a) Principle Component Analysis plot of RNA sequencing results of the MCF10A or HA overproducing cells. **b)** Heatmap of z-score normalized gene expression of differentially expressed genes with hierarchical clustering of both samples and genes. **c)** Gene Set Enrichment Analysis of the Hallmarks gene signature database for genes upregulated in either HAS2 or HAS3 overexpressing cells contrasted against Parental MCF10A cells. **d)** Gene Set Enrichment Analysis of published HIF1α target genes for HAS2 or HAS3 overexpressing cells. All results are not significant. (FDR q-values ≥ 0.25) **e)** Venn diagram displaying the total number of significantly increased genes (FDR ≤ 0.05, log2(Fold Change) ≥ 1) in either HAS2 or HAS3 overexpressing cells. The top 4 most significant genes excluding HAS2/3 are shown in the table. **f)** Ranked enrichment analysis of a curated list of

migration and metabolism gene sets for tumors from the METABRIC cohort. The degree of enrichment is determined as the $-\log_{10}$(p-value) multiplied by the sign of the difference in enrichment scores (ES) of patients stratified into either low or high enrichment of the HA overproduction gene signature. The dashed red line denotes the empirically determined cutoff for non-random enrichment. **g)** METABRIC patient survival probability predicted by the overlapping 72-gene signature of HA overexpressing cells. Patient signature scores were stratified into quartiles, and a log-rank test was used to determine statistical significance.